NASA/TM—2016-219105

Cyclic Oxidation and Hot Corrosion of NiCrY-Coated Disk Superalloys

Timothy P. Gabb
Glenn Research Center, Cleveland, Ohio

Robert A. Miller
Vantage Partners, LLC, Brook Park, Ohio

Chantal K. Sudbrack, Susan L. Draper, James A. Nesbitt, Richard B. Rogers, and Ignacy Telesman
Glenn Research Center, Cleveland, Ohio

Vanda Ngo
University of Arizona, Tucson, Arizona

Jonathan Healy
Vantage Partners, LLC, Brook Park, Ohio

June 2016

NASA STI Program . . . in Profile

Since its founding, NASA has been dedicated to the advancement of aeronautics and space science. The NASA Scientific and Technical Information (STI) Program plays a key part in helping NASA maintain this important role.

The NASA STI Program operates under the auspices of the Agency Chief Information Officer. It collects, organizes, provides for archiving, and disseminates NASA's STI. The NASA STI Program provides access to the NASA Technical Report Server—Registered (NTRS Reg) and NASA Technical Report Server—Public (NTRS) thus providing one of the largest collections of aeronautical and space science STI in the world. Results are published in both non-NASA channels and by NASA in the NASA STI Report Series, which includes the following report types:

- TECHNICAL PUBLICATION. Reports of completed research or a major significant phase of research that present the results of NASA programs and include extensive data or theoretical analysis. Includes compilations of significant scientific and technical data and information deemed to be of continuing reference value. NASA counter-part of peer-reviewed formal professional papers, but has less stringent limitations on manuscript length and extent of graphic presentations.

- TECHNICAL MEMORANDUM. Scientific and technical findings that are preliminary or of specialized interest, e.g., "quick-release" reports, working papers, and bibliographies that contain minimal annotation. Does not contain extensive analysis.

- CONTRACTOR REPORT. Scientific and technical findings by NASA-sponsored contractors and grantees.

- CONFERENCE PUBLICATION. Collected papers from scientific and technical conferences, symposia, seminars, or other meetings sponsored or co-sponsored by NASA.

- SPECIAL PUBLICATION. Scientific, technical, or historical information from NASA programs, projects, and missions, often concerned with subjects having substantial public interest.

- TECHNICAL TRANSLATION. English-language translations of foreign scientific and technical material pertinent to NASA's mission.

For more information about the NASA STI program, see the following:

- Access the NASA STI program home page at http://www.sti.nasa.gov

- E-mail your question to help@sti.nasa.gov

- Fax your question to the NASA STI Information Desk at 757-864-6500

- Telephone the NASA STI Information Desk at 757-864-9658

- Write to:
  NASA STI Program
  Mail Stop 148
  NASA Langley Research Center
  Hampton, VA 23681-2199

NASA/TM—2016-219105

Cyclic Oxidation and Hot Corrosion of NiCrY-Coated Disk Superalloys

Timothy P. Gabb
Glenn Research Center, Cleveland, Ohio

Robert A. Miller
Vantage Partners, LLC, Brook Park, Ohio

Chantal K. Sudbrack, Susan L. Draper, James A. Nesbitt, Richard B. Rogers, and Ignacy Telesman
Glenn Research Center, Cleveland, Ohio

Vanda Ngo
University of Arizona, Tucson, Arizona

Jonathan Healy
Vantage Partners, LLC, Brook Park, Ohio

Prepared for the
Materials Science & Technology 2015
sponsored by the MS&T
Columbus, Ohio, October 4–8, 2015

National Aeronautics and
Space Administration

Glenn Research Center
Cleveland, Ohio 44135

June 2016

Acknowledgments

This Advanced Air Transport Technology Project was sponsored by the
Advanced Air Vehicles Program at the NASA Glenn Research Center.

Level of Review: This material has been technically reviewed by technical management.

Available from

NASA STI Program
Mail Stop 148
NASA Langley Research Center
Hampton, VA 23681-2199

National Technical Information Service
5285 Port Royal Road
Springfield, VA 22161
703-605-6000

This report is available in electronic form at http://www.sti.nasa.gov/ and http://ntrs.nasa.gov/

Cyclic Oxidation and Hot Corrosion of NiCrY-Coated Disk Superalloys

Timothy P. Gabb
National Aeronautics and Space Administration
Glenn Research Center
Cleveland, Ohio 44135

Robert A. Miller
Vantage Partners, LLC
Brook Park, Ohio 44142

Chantal K. Sudbrack, Susan L. Draper, James A. Nesbitt,
Richard B. Rogers, and Ignacy Telesman
National Aeronautics and Space Administration
Glenn Research Center
Cleveland, Ohio 44135

Vanda Ngo
University of Arizona
Tucson, Arizona 85721

Jonathan Healy
Vantage Partners, LLC
Brook Park, Ohio 44142

Abstract

Powder metallurgy disk superalloys have been designed for higher engine operating temperatures through improvement of their strength and creep resistance. Yet, increasing disk application temperatures to 704 °C and higher could enhance oxidation and activate hot corrosion in harmful environments. Protective coatings could be necessary to mitigate such attack. Cylindrical coated specimens of disk superalloys LSHR and ME3 were subjected to thermal cycling to produce cyclic oxidation in air at a maximum temperature of 760 °C. The effects of substrate roughness and coating thickness on coating integrity after cyclic oxidation were considered. Selected coated samples that had cyclic oxidation were then subjected to accelerated hot corrosion tests. This cyclic oxidation did not impair the coating's resistance to subsequent hot corrosion pitting attack.

Introduction

Powder metallurgy (PM) disk superalloys have been designed for higher engine operating temperatures through improvement of their strength and creep resistance. This has required increases in volume fraction of the strengthening γ' phase. Increased amounts of refractory elements such as Ti, Ta, W, Nb have also been included, to strengthen both the γ' and γ phases. In order to maintain the desired proportions and stability of these phases, the addition of these elements have required reductions in other elements, including Cr and Al which are known to provide environmental resistance (Ref. 1). Yet, increasing disk application temperatures to 700 °C and higher could enhance oxidation and also activate hot corrosion in harmful environments.

Studies have shown that oxidation from exposures at 700 °C and higher can impair the mechanical fatigue resistance of disk superalloys (Refs. 2 and 3). This has been related to the formation of oxide layers and changes in superalloy chemistry adjacent to the oxide layers. Concerning these oxide layers, nickel, cobalt, and titanium oxides are considered not protective. There are also corresponding changes in the composition and microstructure of the superalloy adjacent to the exposed surface (Refs. 4 and 5), including a zone of weakened gamma phase without gamma prime precipitates that can be recrystallized to a finer grain size than the original disk alloy grains. Collectively, these features can lower the mechanical fatigue resistance at the surface of disk superalloys.

Hot corrosion of superalloys has been extensively reviewed (Refs. 6 and 7). Type II hot corrosion attack can occur at 700 °C to nearly 800 °C on disk superalloys by the melting of ingested deposits containing mixtures of sodium-, magnesium-, and calcium- sulfates, as well as by direct impingement of SO_2-containing exhaust gas environments. Here, surface oxides go into solution and rendered non-protective through attack by the liquid sulfates, and one of several proposed mechanisms of penetration by continued oxide reduction can occur. The attack can sometimes be further enhanced at the grain boundaries in superalloys. Pits can form in some conditions, while general corrosion can otherwise occur (Ref. 6). Pits can act as stress concentration sites, which encourage cracks to initiate during mechanical fatigue loading. This can significantly reduce the fatigue resistance of disk superalloys (Refs. 3, 8, 9, 10, and 11).

The application of metallic coatings to protect exposed disk surfaces at susceptible locations is a potential solution to these forms of attack, but this introduces other challenges. Such a coating must of course provide continuous protection from this oxidation and corrosion for relevant temperatures and environments. However, it is essential that the coating must not impair the mechanical properties and functions of the rotating disk, which is subjected to high thermal strains and cyclic stresses in each flight or service cycle. This dictates that a properly constituted and applied coating must not harm either the thermal or mechanical fatigue resistance of the disk surfaces upon which it is applied. These disk surfaces would have varied contours and line of sight access for coating as well as varied machining/surface finishes, which could induce variations in coating thickness and roughness. In early trials of applying ductile NiCrY coatings to specimens, mechanical fatigue at high temperatures of 704 to 760 °C promoted enhanced cracking of the coating (Fig. 1). This suggested thermal fatigue could be an issue. The objective of the study was to determine the effects of substrate roughness and coating thickness on oxidation during thermal cycling and on subsequent corrosion resistance, for two powder metal disk superalloys protected by a nickel-chromium-yttrium (NiCrY) coating.

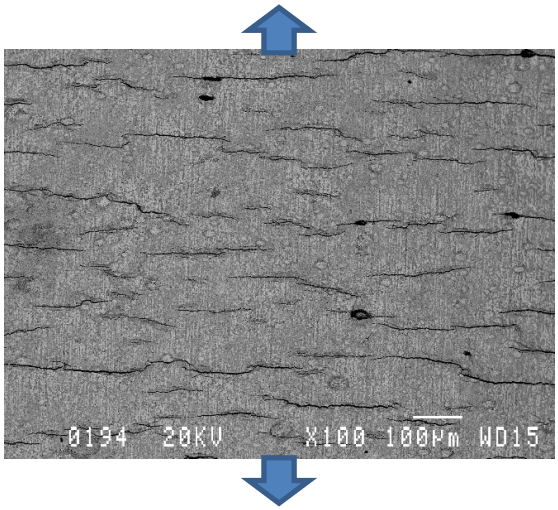

Figure 1.—Cracking of this NiCrY coating on ME3 with low stress ground and polished substrate finish induced in preliminary evaluations by mechanical fatigue cycling to failure at 760 °C. The loading direction was vertical.

Materials and Procedure

A nickel-chromium-yttrium coating was deposited on PM disk superalloys LSHR and ME3 in one run for this study. The LSHR and ME3 test materials had the compositions listed in Table 1. LSHR superalloy powder was atomized in argon by Special Metals, PCC, screened to –270 mesh, sealed in a stainless steel container, and then consolidated by hot isostatic pressing, extruded, and then segments were isothermally forged into flat disks. Rectangular blanks about 13 mm square and 66 to 83 mm long were extracted from as-forged disks of LSHR. These blanks were supersolvus solution heat treated at 1171 °C for 2 h in a resistance heating furnace, then cooled in static air at an average cooling rate of 72 °C per min. They were subsequently aging heat treated at 855 °C for 4 h, followed by 775 °C for 8 h. Specimens were metallographically prepared and swab-etched in Waterless Kalling's reagent to inspect typical grain microstructures. LSHR had an average linear intercept grain size of 15 μm, as shown in Figure 2. Cylindrical specimens 6.4 mm in diameter were then machined, as shown in Figure 3(a). ME3 powder was processed in a comparable manner, but was consolidated by hot compaction. Forged ME3 disks were heat treated at similar temperatures to LSHR, as described in Reference 10. Cylindrical specimens also 6.4 mm in diameter were then machined from near the rims of the ME3 disks. ME3 had average linear intercept grain size of 28 μm, as also shown in Figure 2.

The specimens were all machined by low stress grinding, but then often further conditioned with different combinations of subsequent surface finishing techniques, as listed in Table 2. A range of surface conditions and roughness were produced, including low stress ground + polished (low roughness and low cold work) up to strongly shot peened (high roughness and high cold work). LSHR specimens were evaluated with low stress grinding and also low stress grinding followed by mechanical abrasive polishing, vapor honing, grit blasting, and electro-polishing. ME3 specimens were given low stress grinding plus mechanical abrasive polishing, followed by shot peening at Metal Improvement Company according to AMS 2432 using conditioned cut stainless steel wire (CCW21) at an intensity of 8 N and coverage of 100 percent, 16 N-200 percent, and 8 A-300 percent. Here, 100 percent coverage indicates 100 percent of the surface area has been impacted, while 200 percent and 300 percent coverage indicates 200 percent and 300 percent of the time of shot peening needed to attain 100 percent coverage has been used (Ref. 12).

TABLE 1.—COMPOSITION IN WEIGHT PERCENT OF THE LSHR AND ME3 TEST MATERIALS

Alloy – weight percent	Al	B	C	Co	Cr	Fe	Hf	Mn	Mo	Ni	Nb	O	Re	Si	S	Ta	Ti	V	W	Y	Zr
LSHR (s)	3.54	0.027	0.045	20.4	12.3	0.1	0.0	0.0	2.71	Bal.	1.49	0.02		0.012	<.0010	1.52	3.45	0.006	4.28	<.0005	0.049
ME3 (s)	3.42	0.022	0.059	20.64	12.92				3.80	Bal.	0.91					2.30	3.58		2.01		0.051

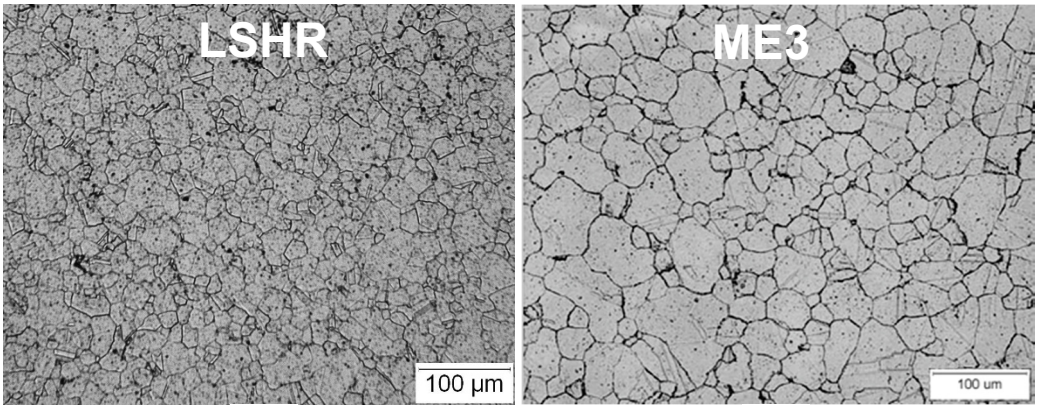

(a) (b)

Figure 2.—Supersolvus solution heat treated plus two step aging heat treated microstructures: (a) LSHR: 15 μm grain size, (b) ME3: 28 μm grain size.

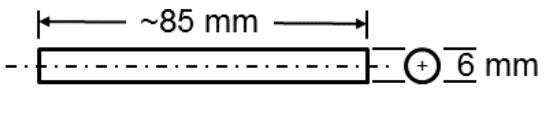

(a)

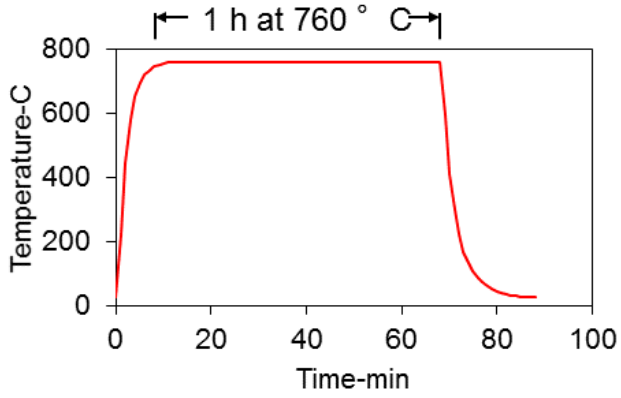

(b)

Figure 3.—Testing details: (a) specimen dimensions, (b) typical time-temperature response during a thermal cycle.

TABLE 2.—SPECIMEN CONDITIONING, TEST CONDITIONS, AND RESULTS. ALL SPECIMENS WERE FIRST LOW STRESS GROUND (LSG), ONLY ME3 SPECIMENS WERE LATER SHOT PEENED (SP)

Relative Roughness, Est. Thickness	ID	Pre-coating Conditioning	Averaged Substrate Roughness (Ra)- µm	Est. Average Coating Thickness (ΔD/2)- µm	Thermal cycles of 25C to 760C/1h	Final Cycled Roughness (Ra)- µm	Final TransSec Coating Thickness- µm	Final TransSec Coating StDev - µm	Mean Oxide Scale Depth- µm	+/- 95% Conf. Int.- µm	Mean Finger Depth- µm	+/- 95% Conf. Int.- µm
-1 -1	11	LSHR- LSG+longitudinal polish	0.24	7.62	1020	0.90	11.68	0.50	0.93	0.02	3.38	0.47
-1 0	7	LSHR- LSG+longitudinal polish+45 psi grit blast	0.32	11.81	1020	0.87	12.34	0.52	1.07	0.02	2.44	0.28
0 0	3	LSHR-LSG+longitudinal polish+85psi grit blast	0.64	11.05	1020	1.00	12.52	0.68	1.18	0.02	2.60	0.41
0 0	4	LSHR- LSG	0.51	12.07	500	1.00	12.01	1.31	0.67	0.01	1.63	0.39
0 +1	6	LSHR- LSG+vapor honed	0.76	14.48	1020	0.86	11.80	0.72	0.72	0.01	4.06	0.88
+1 0	10x	LSHR- LSG+85 psi grit blast	1.07	11.94	1020	1.00	12.30	0.45	0.97	0.01	1.95	0.38
0 0	2	ME3-LSG+longitudinal polish+SP8N-100%	0.81	12.32	1020	1.22	12.31	0.76	1.01	0.02	2.85	0.49
+1 -1	8	ME3-LSG+longitudinal polish+SP16N-200%	1.17	9.14	1020	1.50	12.83	0.78	1.00	0.01	1.87	0.54
+1 +1	9	ME3-LSG+longitudinal polish+SP8A(~24N)-300%	1.50	17.27	1020	1.84	13.28	0.49	0.69	0.01	2.07	0.44

High Power Impulse Magnetron Sputtering (HiPIMS) was employed by Southwest Research Institute to apply a Ni-35Cr-0.15Y (weight percent, nominal) coating. The coating was applied at consistent conditions for all specimens. The specimens were usually held by one end in a sleeve on a double rotation, planetary fixture to allow uniform coating thicknesses on the individual samples.

Thermal cycling exposures were conducted in air on these coated specimens. All specimens were heated to 760 °C and cooled to 25 °C each thermal cycle. The specimens were suspended horizontally from an alumina tube while a resistance-heating tube furnace automatically translated over the specimens

during the 60 min heating cycle. The furnace automatically translated away from the specimens during the 20 min cooling cycle. A typical heating and cooling cycle is shown in Figure 3(b), showing outputs from an attached platinum–rhodium "Type R" thermocouple. These specimens were exposed to 500 cycles, and then removed for examination. Most specimens were later given 520 more thermal cycles, for a total of 1,020 cycles and 1,020 accumulated hours at 760 °C, as listed in Table 2.

Each coated specimen was examined using a JEOL 6100 scanning electron microscope (SEM) at up to 1000x magnification first as-coated, and later after heat treatment at 760 °C for 8 h in a low partial pressure of oxygen, the starting condition before cyclic oxidation exposures. They were then later examined after 500 and 1,020 thermal cycles. Average roughness was measured on the uncoated pins after the surfaces were prepared, and after completion of coating, heat treatment, plus thermal cycling using an optical profiler, the Zygo NewView 7200 white light interferometer, with a 10x objective lens magnification having a resolution of 0.001 μm. Average diameters of each pin were measured before and after coating, before heat treatment or cyclic oxidation, using a dual axis optical micrometer Beta LaserMike Accuscan 5025-RS232, having a resolution of 0.01 μm. Residual stresses on the coating surface were measured using a Bruker D8 Discover (area detector) x-ray diffractometer aligned in accordance with ASTM E 915, using a Mn target and the (311) crystallographic plane on a specimen target area of 1.2 mm^2. These results were analyzed using the Bruker LEPTOS v.7 software.

After completion of these measurements, transverse sections were sliced from each coated specimen, sputtered with a thin layer of gold, plated with a protective nickel coating, and metallographically prepared. The unetched metallographic sections were then examined in an Hitachi 4700 field emission scanning electron microscope (FESEM), where the surfaces were consistently imaged using a backscattered electron detector, sensitive to the changes in average atomic number between different coating and oxide layers. Coating phases and their compositions were screened on several specimens using a JEOL JXA-8200 scanning electron microprobe, including wavelength dispersive X-ray spectrometry.

A remaining coated section of each specimen was then subjected to an accelerated hot corrosion test. These specimen sections were corroded in air, by first coating them with a salt mixture of 60 wt% Na_2SO_4-40 wt% $MgSO_4$ salt layer applied at 2 mg/cm^2 and then suspending them horizontally in a resistance-heating tube furnace at 760 °C for 50 h. While this salt mixture does not represent an ideal eutectic mixture of these two constituents having the lowest melting temperature, it had been observed in numerous trials, when applied as a thin layer on these disk superalloys, to melt in a furnace held at 700 °C to 760 °C and promote the nucleation and growth of corrosion pits on the uncoated LSHR and ME3 superalloy surfaces within 24 h, as shown in Figure 4. The coated specimens which were corroded in this way were then examined in the SEM for the presence of pits.

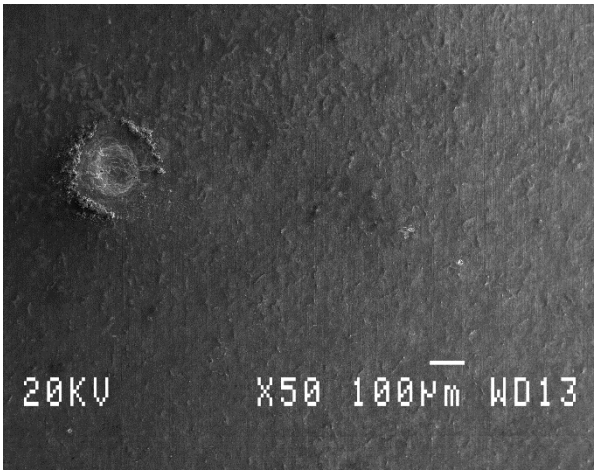

Figure 4.—Typical corrosion pit among many observed on an unprotected surface of LSHR, after the accelerated corrosion test.

Results and Discussion

A significant range of average roughness (R_a) values of 0.24 to 1.50 µm R_a were obtained for the variously prepared superalloy specimens to be coated. It was intended that they be coated equivalently. However, resulting coating thickness as estimated by the change in uncoated versus coated diameter ($\Delta D/2$) varied from 7.6 to 17.3 µm for different specimens. Substrate roughness versus estimated coating thickness is shown in Figure 5 for the six LSHR and three ME3 specimens that were prepared, indicating varied combinations were obtained. Typical SEM images showing the surfaces of coated LSHR and ME3 specimen surfaces at comparable roughness and estimated coating thickness values near mid-range (red box) are shown in Figure 6. For each shown condition of as-heat treated, after 500 thermal cycles, and after 1,020 thermal cycles, the coated surfaces compared very well in appearance and coated surface composition between the two alloys, and could be considered essentially the same. Spits, or coating nodules, were observed to be scattered on the surfaces for all cases, having the same Cr_2O_3 oxide composition as the surrounding surface. Taken together, coated LSHR and ME3 specimens gave a range of substrate roughness and estimated coating thickness values, and the measured (roughness, thickness) variables for coated LSHR plus ME3 were sufficiently balanced for making comparisons. As shown in Figure 7, specimens with extreme combinations of pre-coat substrate roughness and estimated coating thickness values were selected to form a template, for consistently comparing images to depict various aspects of the test results.

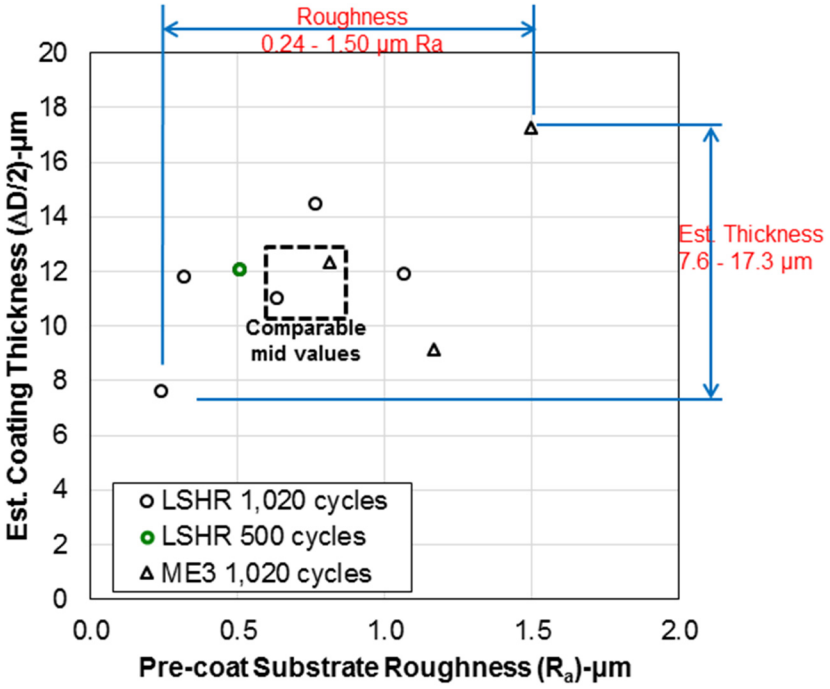

Figure 5.—Average substrate roughness versus estimated coating thickness values attained for the coated pins, with coating thickness estimated after coating and before cyclic oxidation by the change in measured diameter.

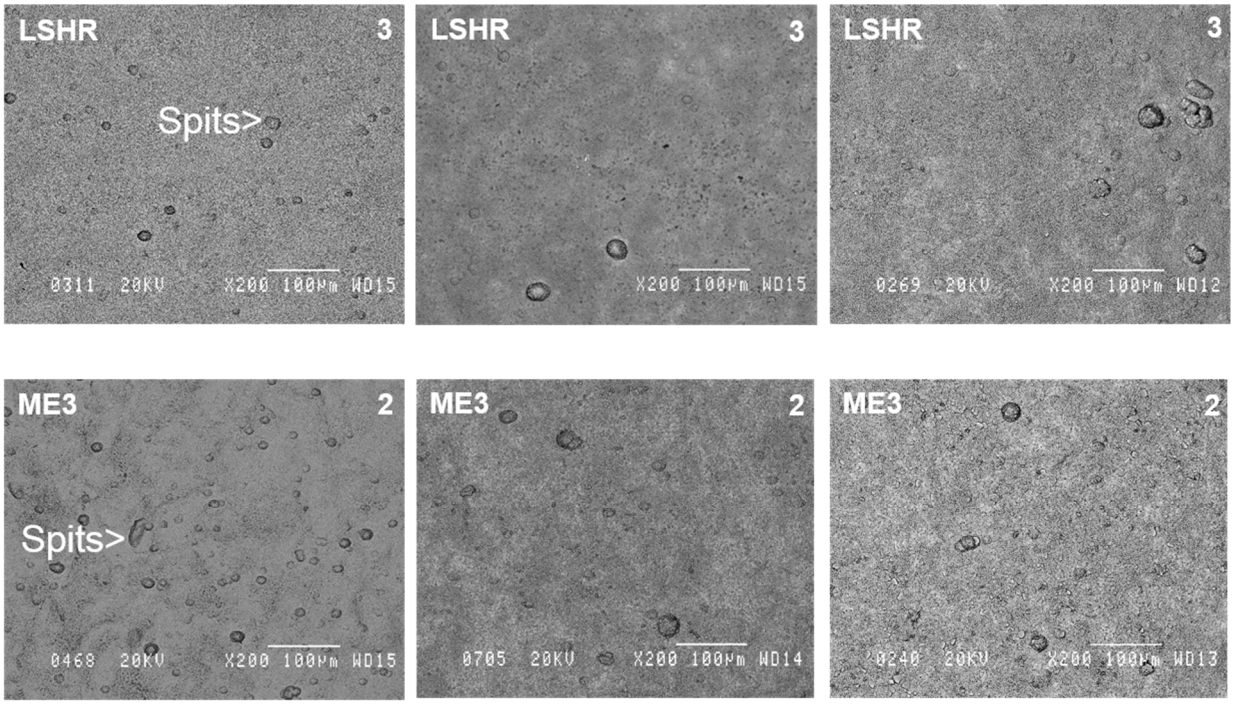

Figure 6.—Comparison of coated LSHR specimen 3 and coated ME3 specimen 2 surfaces having comparable pre-coat substrate roughness and estimated coating thickness values near mid-range, as indicated in Figure 5: (a) as-heat treated, (b) after 500 thermal cycles, and (c) after 1,020 thermal cycles.

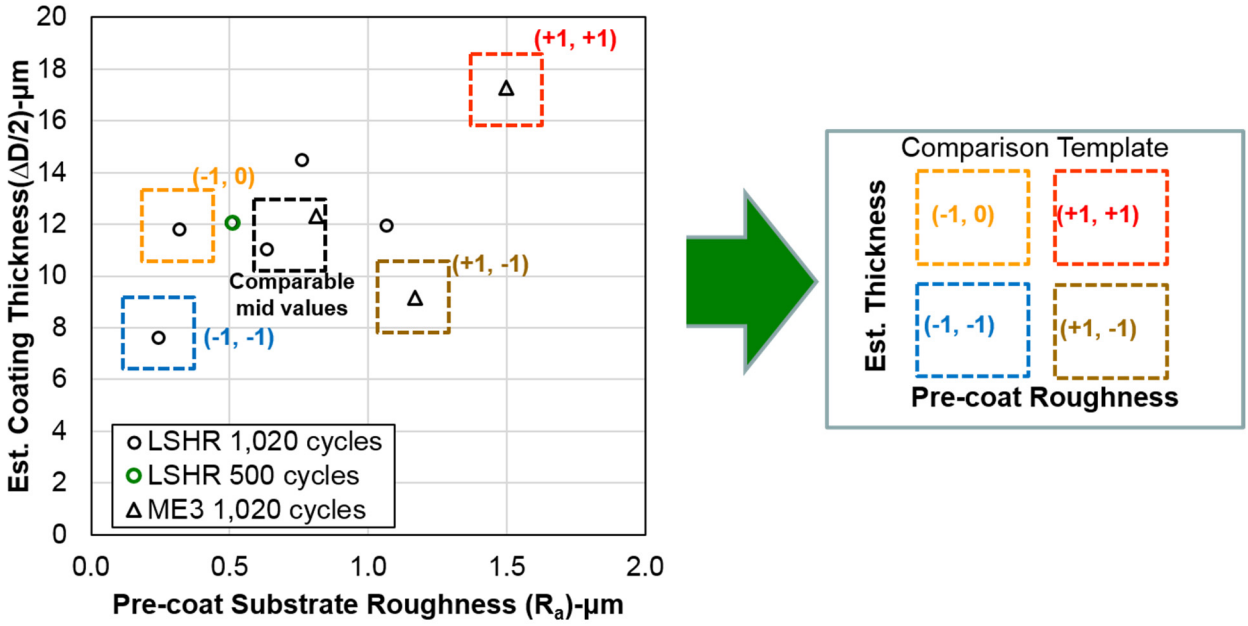

Figure 7.—LSHR and ME3 specimens' pre-coat substrate roughness and estimated coating thickness values, showing the measured (roughness, thickness) variables were sufficiently balanced for comparisons at extreme values of pre-coat substrate roughness and estimated coating thickness. The –1 and +1 nomenclature indicates values near the minimum and maximum observed for each variable.

A comparison of the specimen surfaces after 1,020 thermal cycles is shown using this template in the backscattered electron (BSE) microscope images of Figure 8. No linear cracking or pealing of the coating was observed, and effects of varied pre-coat substrate roughness and estimated coating thickness were not observed. Cr_2O_3 oxide predominated on the specimen surface, based on energy dispersive x-ray analyses in the SEM. The spits appeared to be stable and still adhered to the surface, and still had the same Cr_2O_3 oxide composition as the surrounding surface. Pre-coat substrate roughness versus coated plus thermally cycled roughness is plotted for all specimens in Figure 9, with estimated thickness labeled in parentheses. Pre-coat substrate roughness and coating roughness after cycling were correlated, but no consistent effect of estimated coating thickness was evident. Average axial and transverse residual stresses in the coating after thermal cycling are shown in Figure 10 for all specimens, with estimated thickness labeled in parentheses. Comparable tensile residual stresses were measured in both axial and transverse directions for all cases, and no significant effects of varied pre-coat substrate roughness and estimated coating thickness were observed.

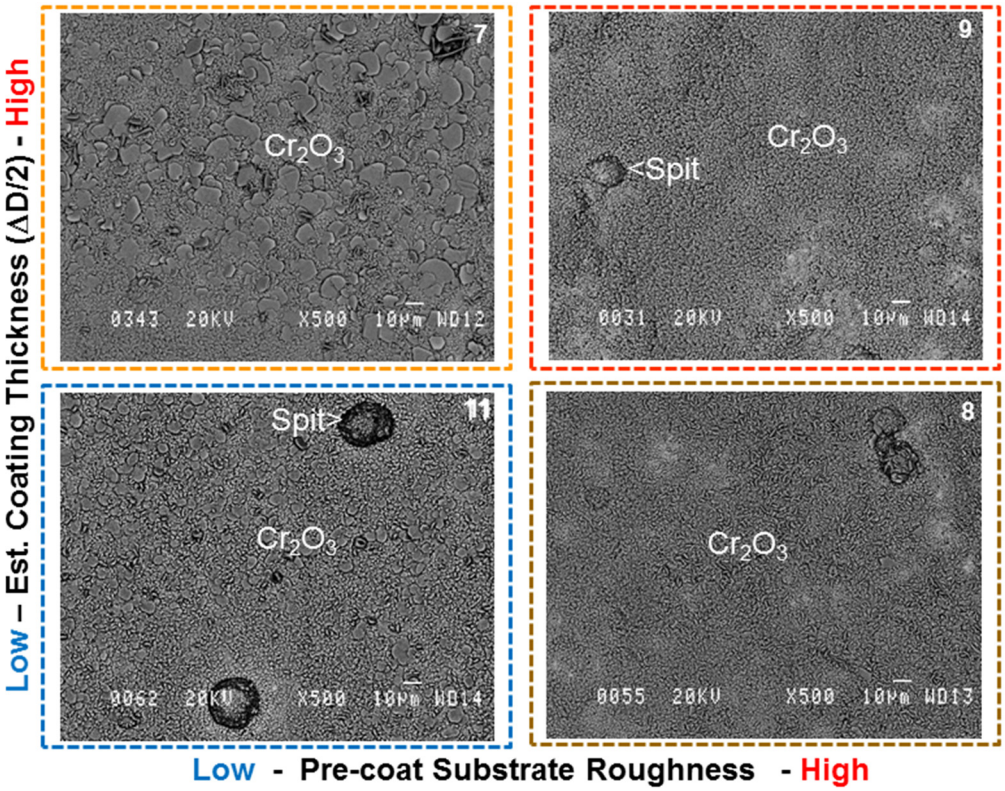

Figure 8.—Comparison of specimen surfaces after 1,020 thermal cycles at extreme values of pre-coat substrate roughness and estimated coating thickness. No linear cracking or pealing of the coating was observed, and effects of varied roughness and coating thickness were not observed.

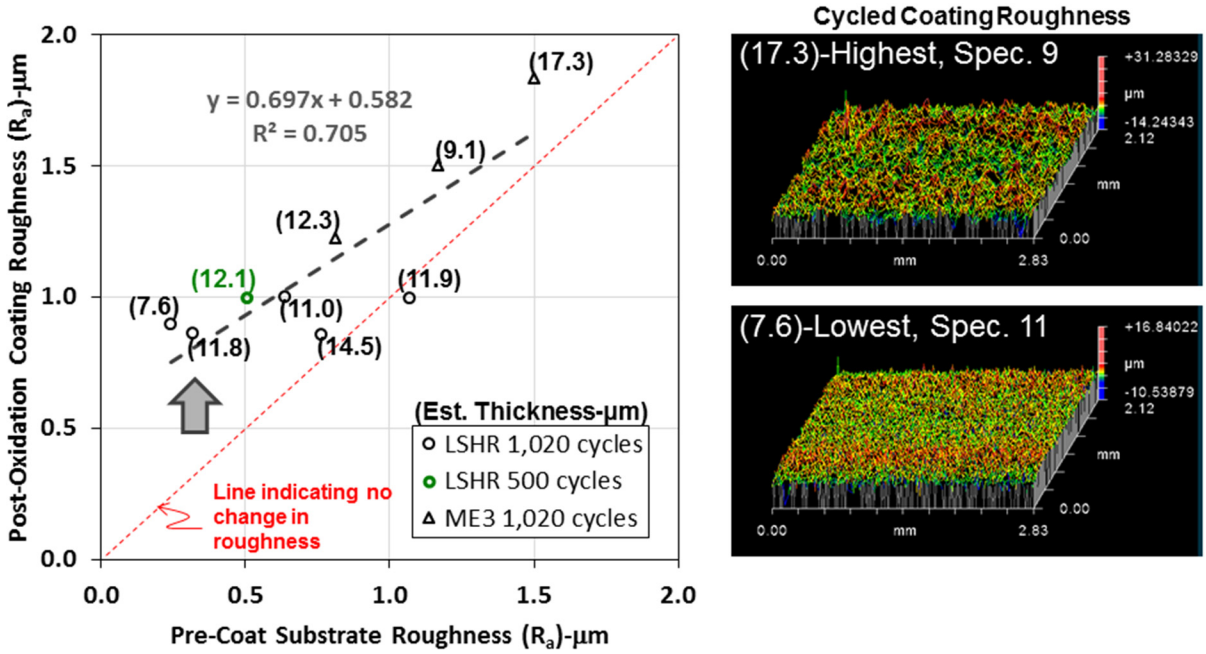

Figure 9.—Pre-coat substrate roughness versus coated, thermally cycled roughness, with estimated thickness labeled in parentheses. Pre-coat substrate roughness and coating roughness after cycling were correlated, but no consistent effect of estimated coating thickness was evident.

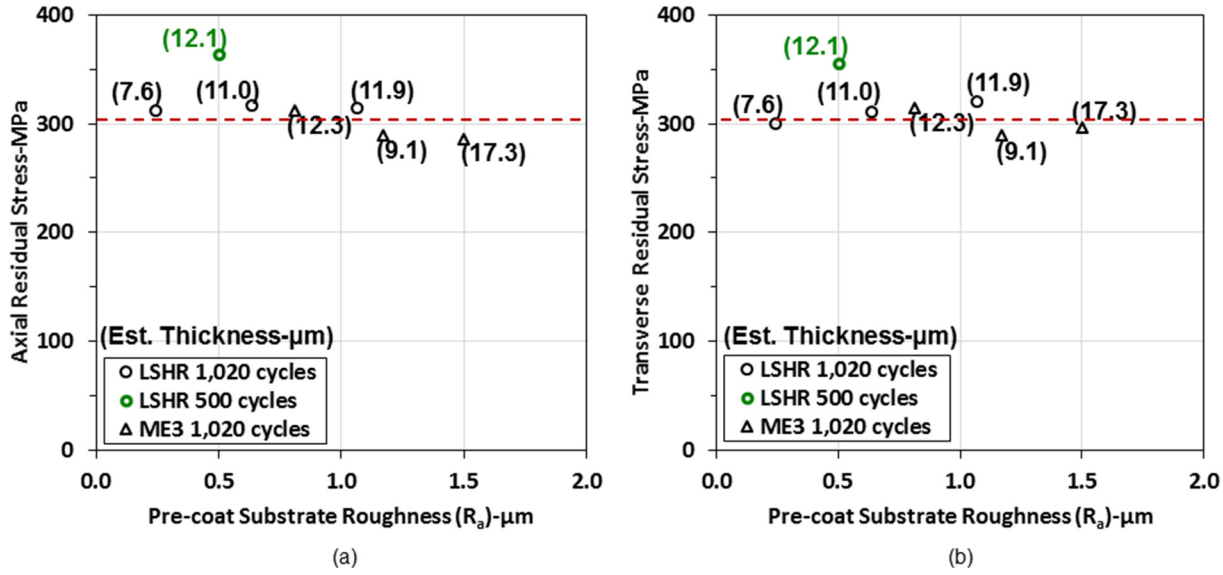

Figure 10.—Average (a) axial and (b) transverse residual stresses in the coating after thermal cycling, with estimated thickness labeled in parentheses. Comparable tensile residual stresses were measured in both axial and transverse directions, and no significant effects of varied pre-coat substrate roughness and estimated coating thickness were observed.

Comparisons of coating-oxide layers in transverse sections are shown for the same extreme cases after 1,020 thermal cycles in Figure 11. The protective coating layer was still continuous, but did have surface oxidation. A continuous outer scale predominantly composed of Cr_2O_3 oxide composition was present, with Al_2O_3 fingers extending in beneath this outer scale. Several Al_2O_3 particles were also identified at the coating-substrate interface, apparently embedded during grit blasting of the pre-coat substrate. It was surprising that the thickness of the coating appeared comparable for these extreme cases. Coating thickness was, therefore, measured for all transverse sections. Initial estimated average thickness versus cycled, actually measured thickness is shown in Figure 12 for all specimens, with pre-coat substrate roughness labeled in parentheses. It was clear that estimations of average coating thickness ($\Delta D/2$) did not only reflect actual differences in coating thickness, but also other factors. Yet, no consistent effect of varied pre-coat substrate roughness on cycled actual coating thickness was observed. Plots of mean layer dimensions versus average pre-coat substrate roughness are shown in Figure 13 for all specimens. No consistent effect of increasing pre-coat substrate roughness was observed on either outer oxide layer thickness or inner finger depth.

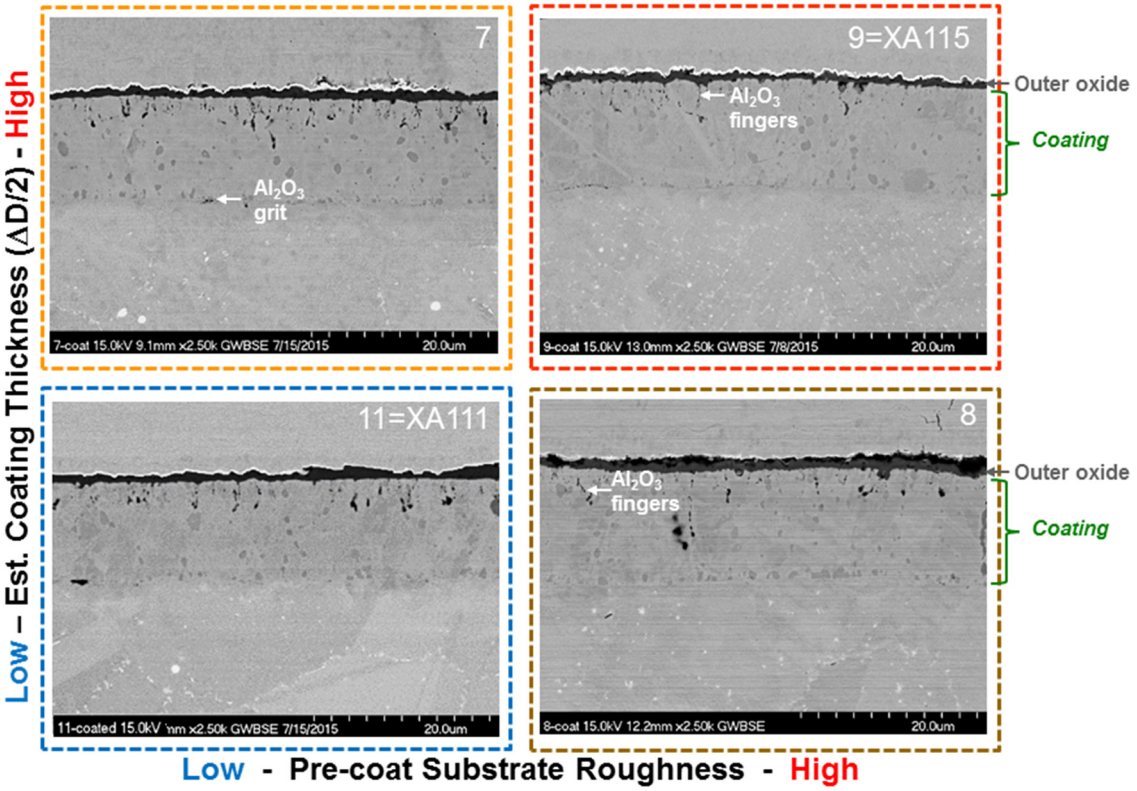

Figure 11.—Comparison of coating-oxide layers in transverse sections after 1,020 thermal cycles at extreme values of pre-coat substrate roughness and estimated coating thickness. The protective coating layer was still continuous and mostly intact, with comparable remaining coating thickness evident for these extreme cases.

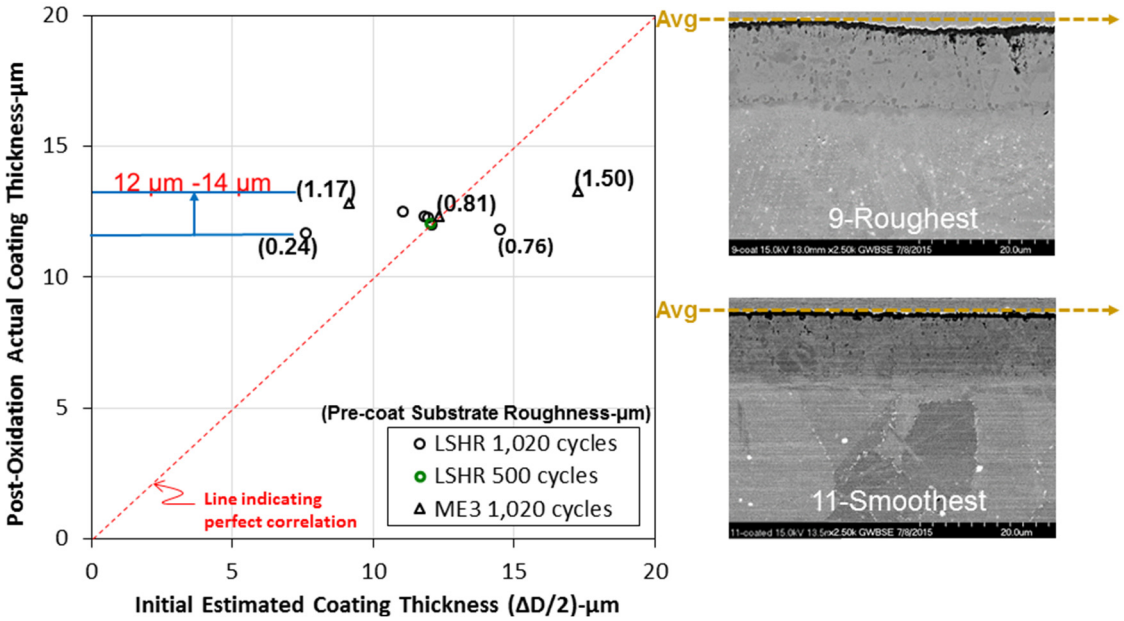

Figure 12.—Initial estimated average coating thickness versus cycled, actually measured thicknesses of 12 to 14 µm for all specimens, with pre-coat substrate roughness labeled in parentheses. Estimations of average coating thickness (ΔD/2) did not correlate with or only reflect actual coating thickness, but also other factors. Yet, varied pre-coat substrate roughness also did not directly correlate with cycled actual coating thickness.

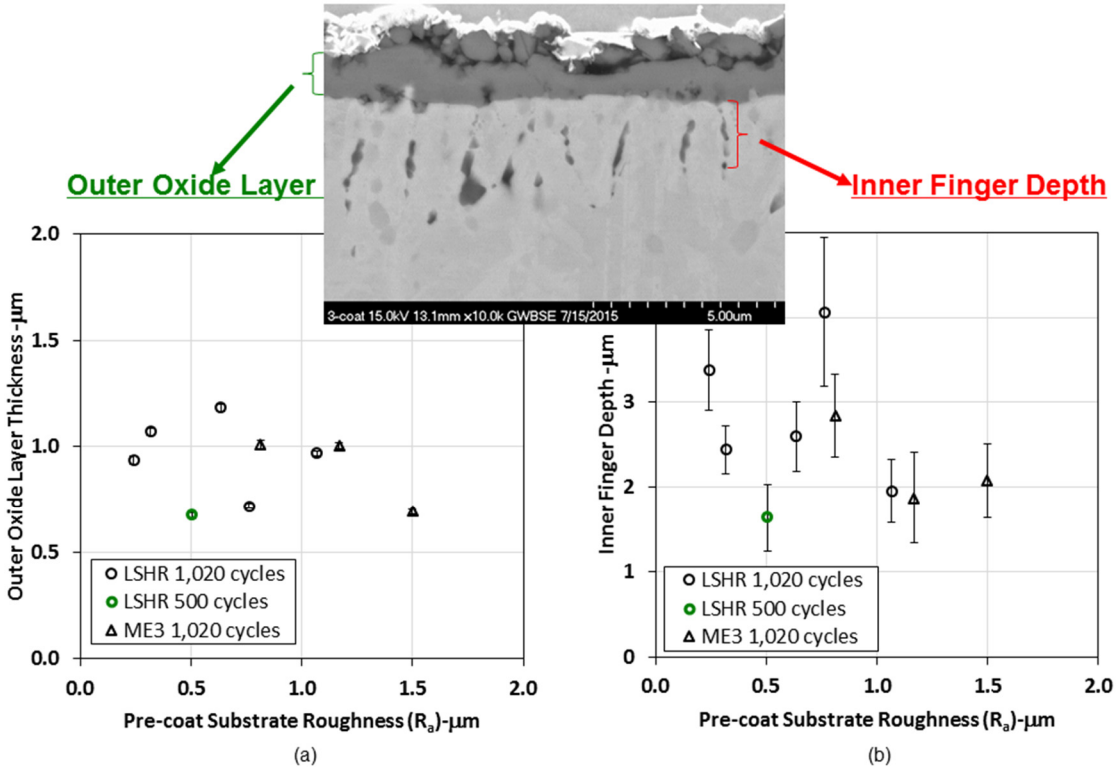

Figure 13.—Plots of mean layer dimensions versus pre-coat substrate roughness for all specimens: (a) outer oxide layer, (b) inner finger depth. No consistent correlation with increasing pre-coat substrate roughness was observed. Vertical bars indicate ±95 percent confidence intervals.

Two SEM images of the coating with the highest roughness (see Fig. 11(b) {pin 9}) are shown at a higher magnification in Figure 14 with the contrast enhanced to clearly show the second phase appearing in the coating. Surprisingly, the particle size of this darker, second phase was not uniformly distributed but consisted of randomly spaced large particles, as those shown in the figure, whereas the smaller particles, typically 0.5 to 2 μm in size, were more uniformly distributed throughout the coating from the coating/LSHR interface to the coating/oxide interface. This phase morphology was typical of coatings on the other samples regardless of surface roughness.

Concentrations of the second phase particles, both the small and larger particles, were measured. Concentrations were approximated from the EDS spectra using standard atomic number, absorption, and fluorescence (ZAF) corrections and using the concentration of the LSHR alloy as a reference standard for all major elements (Ni, Co, Cr, Al, Ti, W, Mo, Ta, Nb) (Ref. 13). Both large and small particles had high Cr concentrations (>90 percent). The most obvious difference between the large and small particles was that the small particles contained higher W, Mo and Ta concentrations (up to 2.7 W, 1.2 Mo, and 0.9 Ta) whereas the highest concentration of W in the larger particles was ~0.7 percent, with all other elements less than 0.5 percent (Ni balance).

Concentrations across the coating (avoiding the second phase particles) were also measured by energy dispersive spectroscopy (EDS). The concentration profile across the coating is shown in Figure 14(c).[1] Whereas the nominal Cr concentration of the coating was 35 percent, the Cr concentration can be seen to have decreased to approximately 32 percent near the oxide scale and slopes downward to the lower-Cr LSHR alloy (nominal concentration of 12.3 Cr). As expected, each of the elements in the LSHR alloy had diffused into the Ni-Cr coating, but only Co could be measured at a concentration above 5 percent.

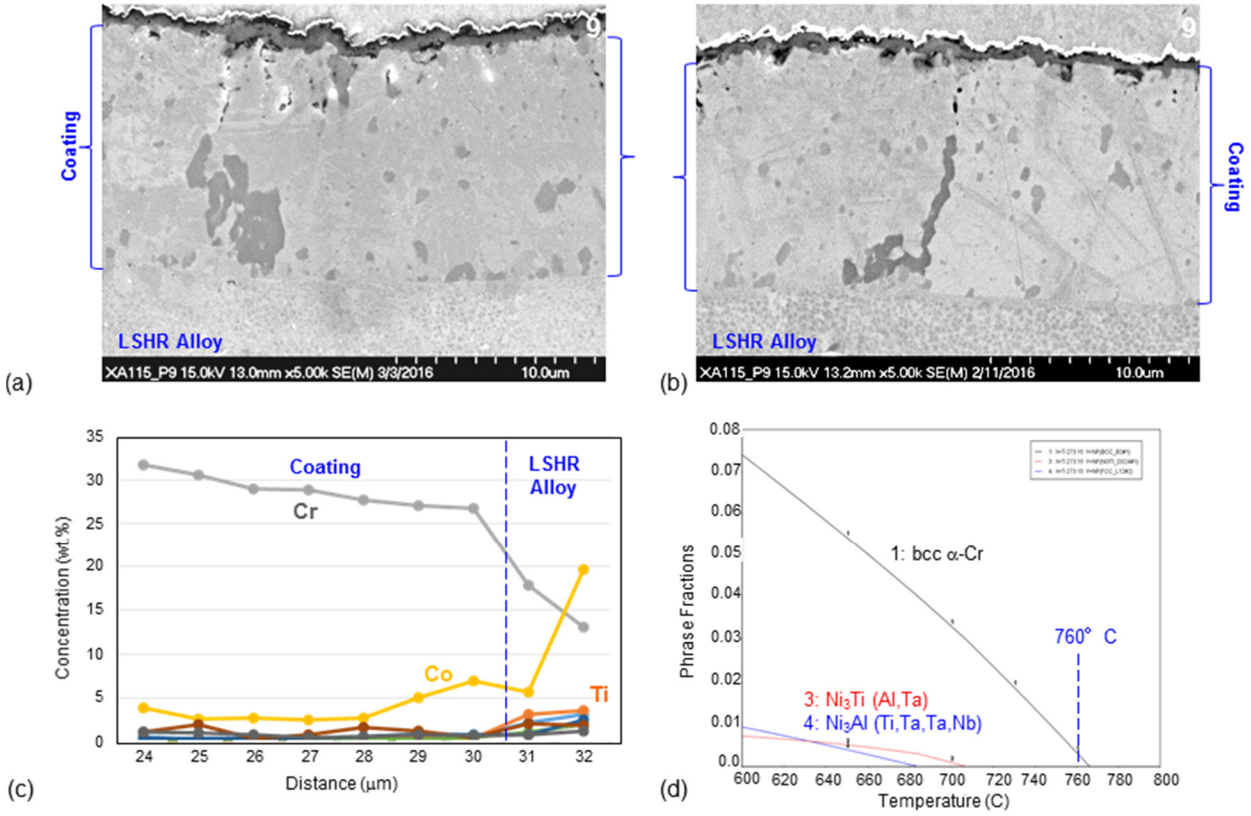

Figure 14.—(a) and (b) SEM micrographs of the coating for specimen 9 shown in Figure 11(b) clearly showing both the large and small dark second phase, (c) EDS concentration profile through the coating, and (d) predicted phase fractions versus temperature for the α-bcc Cr phase and the $Ni_3(Al,Ti)$ ordered L12 phase.

[1] All concentrations are given in weight percent.

The high Cr concentration indicates the dark phase is the α-bcc Cr phase, although it is curious that it appears even after the Cr concentration in the coating was reduced. It is content and size range in as-deposited coatings near this concentration is currently being studied. To investigate whether the thermal cycling or the diffusion of elements from the LSHR alloy into the coating might be stabilizing the α-bcc Cr phase, a typical composition in the coating was investigated using the thermodynamic modeling program Thermo-Calc (Ref. 14) with the TCS Ni-Alloys database v7.1 (Ref. 15). A representative composition of the Ni solid solution phase in the middle of the coating was taken from the data in Figure 14(c) (Ni: 63.8, Co: 1.9, Cr: 31.9, Al: 0.3, Ti: 0.2, W: 1.1, Mo: 0.2, Ta: 0.5, Nb: 0.1). This composition did not include the Cr residing in the α-Cr phase. At 760 °C, for the above concentration, a small amount (<1 percent) of the α-bcc Cr phase is predicted. By scanning each of the elements while holding all others constant, it was seen that Cr, as well as the elements Al, Ti, Ta, Nb and W all stabilize the α-bcc phase, Mo has almost no effect while Co destabilizes the phase. Decreases in temperature also stabilizes the α phase, as shown in Figure 14(d). Hence, if the Cr present in the α-bcc phase had been added to the coating composition used above, the predicted volume fraction of the α-bcc Cr phase would have been higher and likely closer to that observed. In addition, as elements in the LSHR substrate diffuse into the coating, most of these elements stabilize the α-bcc Cr phase which accounts for the continued appearance of the phase even though the Cr concentration is decreasing. Furthermore, since lower temperatures also stabilize the phase, thermal cycling the coating could also have an impact on this phase. Slower heating and cooling cycles would favor higher volume fractions of the phase. It would be interesting to evaluate this coating after giving it a longer anneal at 760 °C followed by a rapid quench.

However, the appearance of both the large and small α-Cr particle distribution is puzzling. Interdiffusion of the elements from the LSHR which stabilize the α-Cr phase should be relatively uniform and therefore would be expected to have little effect on the particle distribution. Perhaps when a random particle gets to a certain larger size, it does not have sufficient time at the elevated temperature for diffusion of Cr from the particle to completely reach the equilibrium volume fraction for the local compositional conditions. On cooling and again on reheating, the particle grows larger, never able to reach thermodynamic equilibrium at the test temperature of 760 °C. Hence, under the thermal cycling conditions of this study, certain random particles may increase in size and never have sufficient time at temperature to shrink and reach thermodynamic equilibrium.

Images of specimen surfaces after 1,020 thermal cycles, plus 50 h of corrosion, with subsequent ultrasonic cleaning in ethanol, are shown in Figure 15 using the comparison template. A higher magnification backscatter electron image (BSE) of a typical sample surface, after the oxidation and corrosion exposure, is shown in Figure 16. The majority of the surface is covered in Cr_2O_3 but there are also areas with different morphology and composition. EDS analysis showed Mg, along with O, Cr, and a small amount of Ni, present in the darker, crystalline looking areas. Mg, from the applied salt, reacted during the corrosion exposure to form a phase on the surface of the samples. The lighter areas are higher in Ni and also have a small amount of Co. The higher Ni content indicates that the coating surface is being imaged in these areas and the Cr_2O_3 is thinner or not present. The oxide was attacked in places, but no open corrosion pits exposing the substrate were observed for the any of the varied coated conditions. It was evident that in spite of the thermal cycling, the coating was still able to protect the superalloy substrate from corrosion attack.

It is interesting that the single coated specimen evaluated after only 500 cycles had comparable responses to all the other specimens given 1,020 cycles. This would suggest that at this point the roughness and residual stresses are stable, while the oxide layers' growth rates are low. However, additional tests at more intervals of thermal cycles would be needed to confirm this. Yet, at least for up to 1,020 thermal cycles, the coating continued to protect the superalloy substrate from oxidation and corrosion attack, for all of the varied substrate surface conditions that were evaluated here.

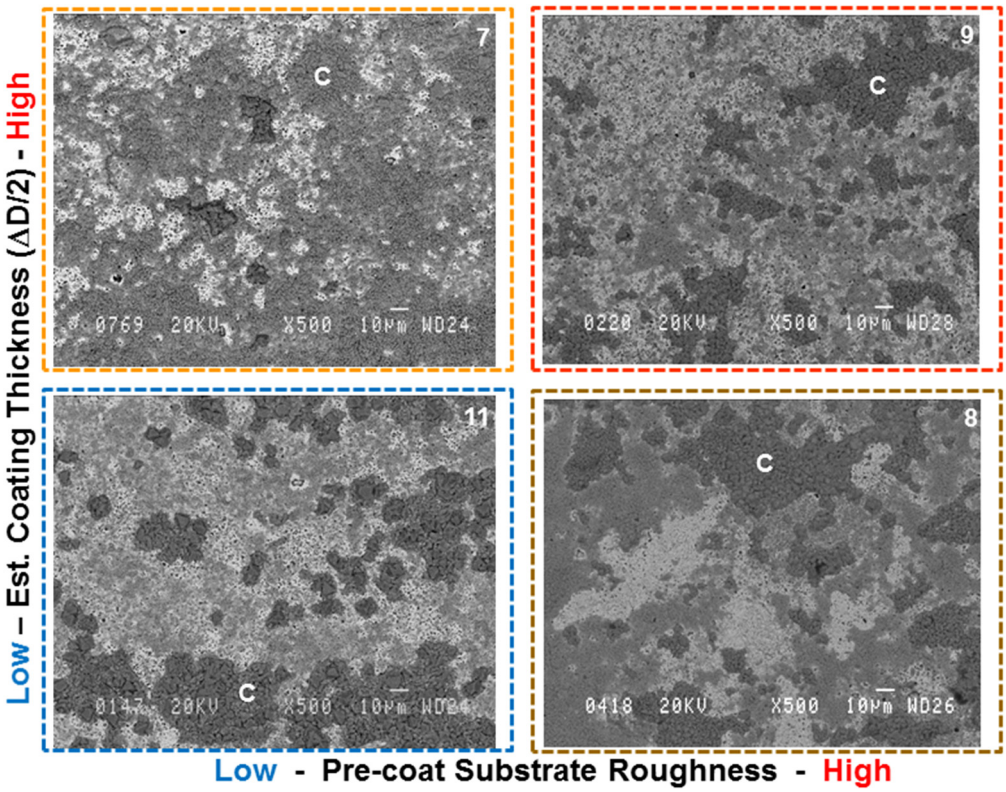

Figure 15.—Comparison of typical coated, cycled, plus corroded surfaces at extreme values of pre-coat substrate roughness and estimated coating thickness. The outer chrome-oxide (C) was attacked to expose underlying layers, but no open corrosion pits protruding into the substrate were observed for the varied coated conditions.

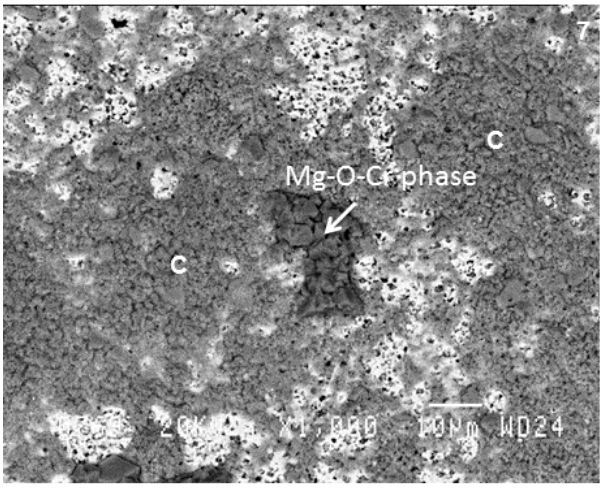

Figure 16.—Back-scattered electron SEM image of pin #7 after oxidation and corrosion exposures. A Mg-O-Cr phase forms during the corrosion exposure. Lighter areas contain higher amounts of Ni and are most likely the coating showing through the chrome-oxide (C) surface.

Summary of Results

LSHR and ME3 substrate specimens were prepared having surface finishes varying average roughness from 0.24 to 1.50 μm, and then coated. This pre-coat substrate roughness correlated with coated, cycled roughness. They were sputter coated with a NiCrY coating to varying estimated thicknesses (ΔD/2) from 7.6 to 17.3 μm. However, the actual coating thicknesses measured in thermally cycled cross sections were much more consistent than estimated, all lying between 12 and 14 μm. They were subjected to up to 1,020 thermal cycles from 25 to 760 °C, and the cyclic oxidation and remaining layers were then measured. No linear cracking or pealing of the coating was observed, with the protective coating layer still continuous and mostly intact under consistent oxide layers that did not strongly vary with roughness. Coated specimen sections were then corroded in air at 760 °C for 50 h. The oxide was attacked, but no open corrosion pits exposing the substrate were observed for the varied substrate-coating conditions.

Conclusions

1. Substrate Roughness: A range of surface conditions with varied roughness on disk surfaces can be consistently sputter coated, including low stress ground + polished (low roughness and low cold work) up to strongly shot peened (high roughness and high cold work).
2. Coating Thickness: Actual coating thicknesses for such different surface conditions can be maintained and remain consistent, however, estimation of coating thickness based on change in average outer dimensions can be tricky for varied surface conditions. Careful calibrations would be necessary using standards having surface conditions consistent with the surfaces to be inspected.
3. Thermal Cycling: The coating for such varied substrate conditions can still consistently resist cyclic oxidation.
4. Corrosion Resistance: This thermally cycled coating can still provide protection from corrosion pitting.

Future Work

The presence and evolution of α phase in the coating with varied processing and exposures will be further studied. The effects of mechanical fatigue on coating effectiveness will also be assessed.

References

1. R.C. Reed, The Superalloys: Fundamentals and Applications, Cambridge University Press, 2008.
2. M.R. Bache, J.P. Jones, G.L. Drew, M.C. Hardy, N. Fox, Environment and time dependent effects on the fatigue response of an advanced nickel based superalloy, Int. J. Fat., V 31 (11-12), Issues 11–12, pp. 1719–1723.
3. A. Encinas-Oropesa, G. Drew, M. Hardy, A. Leggett, J. Nicholls, and N. Simms, Effects of Oxidation and Hot Corrosion in a Nickel Disc Alloy, Superalloys 2008, The Mining, Metallurgy, and Materials Society, Warrendale, PA, 2008, pp. 609–618.
4. J.L. Smialek, P.J. Bonacuse, "Compositional Effects on the Cyclic Oxidation Resistance of Conventional Superalloys," Materials at High Temperatures, published online April 11, 2016.
5. C.K. Sudbrack, S.L. Draper, T. Gorman, J. Telesman, T.P. Gabb, D.R. Hull, "Oxidation and the Effects of High Temperature Exposures on Notched Fatigue Life of an Advanced Powder Metallurgy Disk Superalloy," Superalloys 2012, E.S. Huron, R.C. Reed, M.C. Hardy, M.J. Mills, R.E. Montero, P.D. Portella and J. Telesman, Eds., TMS, Warrendale, PA, 2012, pp. 863–872.
6. R.A. Rapp, Hot Corrosion of Materials: A Fluxing Mechanism?, Corros. Sci., 2002, 44, pp. 209–221
7. F.S. Pettit and C.S. Giggins, Hot Corrosion, Superalloys II, C.T. Sims, N.S. Stoloff, and W.C. Hagel, Eds., John Wiley & Sons, New York, 1987, pp. 327–358

8. J.R. Groh and R.W. Duvelius, Influence of Corrosion Pitting on Alloy 718 Fatigue Capability, Superalloy 718, 625, 706 and Derivatives, E.A. Loria, Ed., The Mining, Metallurgy, and Materials Society, Warrendale, PA, 2001, pp. 583–592.
9. G.S. Mahobia, N. Paulose, S.L. Mannan, R.G. Sudhakar, K. Chattopadhyay, N.C.S. Srinivas, Effects of Hot Corrosion on the Low Cycle Fatigue Behavior of IN718, Int. J. Fat., V. 59, 2014, pp. 272–281.
10. T.P. Gabb, J. Telesman, B. Hazel, D.P. Mourer, The Effects of Hot Corrosion Pits on the FatigueResistance of a Disk Superalloy, J. Mat. Eng. Perf., V. 19(1), 2010, pp. 77–89.
11. J.K. Sahu, R.K. Gupta, J. Swaminathan, N. Paulose, S.L. Mannan, "Influence of Hot Corrosion on the Low Cycle Fatigue Behavior of SU 263," Int. J. Fat., V. 51, 2013, pp. 68–73.
12. J. Cammett, "Shot Peening… Getting It Right," The Shot Peener, Spring 2007, pp. 8–14.
13. IXRF Systems, Inc., 10421 Old Manchaca Rd., Suite 620, Austin, TX 78748 (http://www.ixrfsystems.com/)
14. J.O. Andersson, T. Helander, L. Höglund, P.F. Shi, and B. Sundman, "Thermo-Calc and DICTRA, Computational Tools for Materials Science," Calphad, V. 26, 2002, pp. 273–312.
15. Thermo-Calc Software Database TCS Ni-Alloys database v7.1.